HHS Public Access

Author manuscript

*Phys Med*. Author manuscript; available in PMC 2017 January 06.

Published in final edited form as:

*Phys Med*. 2016 January ; 32(1): 12–22. doi:10.1016/j.ejmp.2015.12.007.

# Advances in time-of-flight PET

**Suleman Surti**[*] and **Joel S. Karp**

Department of Radiology, University of Pennsylvania, Philadelphia, PA 19104, USA

## Abstract

This paper provides a review and an update on time-of-flight PET imaging with a focus on PET instrumentation, ranging from hardware design to software algorithms. We first present a short introduction to PET, followed by a description of TOF PET imaging and its history from the early days. Next, we introduce the current state-of-art in TOF PET technology and briefly summarize the benefits of TOF PET imaging. This is followed by a discussion of the various technological advancements in hardware (scintillators, photo-sensors, electronics) and software (image reconstruction) that have led to the current widespread use of TOF PET technology, and future developments that have the potential for further improvements in the TOF imaging performance. We conclude with a discussion of some new research areas that have opened up in PET imaging as a result of having good system timing resolution, ranging from new algorithms for attenuation correction, through efficient system calibration techniques, to potential for new PET system designs.

### Keywords

PET; Time-of-flight PET; Image quality; Scintillators; Photo-sensors; Image reconstruction

## Introduction

Since the introduction of early ring systems almost 40 years ago, positron emission tomography (PET) has seen considerable advancements in the areas of instrumentation as well as algorithms for image generation. Advancements in the development and utilization of new scintillation detectors have led to improved system spatial resolution and sensitivity. In addition, improved detector performance, development of new and more efficient image reconstruction algorithms, and better computational resources have allowed the migration from 2D systems with septa to fully-3D systems (with no septa) and larger axial fields-of-view, thereby providing further improvements in system sensitivity.

Finally, the combination of a computed tomography (CT) scanner with the PET instrument for both attenuation correction and anatomical correlation has led to widespread implementation of PET/CT in the clinic. The combination of whole-body PET/CT instruments with $^{18}$F-FDG has helped PET to become a mainstream tool for the diagnosis

[*]Corresponding author. Department of Radiology, Perelman School of Medicine, University of Pennsylvania, 156B John Morgan Building, 3620 Hamilton Walk, Philadelphia, PA 19104, USA. Tel.: +1 215 573 5460; fax: +1 215 573 3880. surti@mail.med.upenn.edu (S. Surti).

and staging of cancer, although the clinical use of PET today also includes $^{82}$Rb imaging to measure cardiac perfusion, with other emerging clinical applications on the horizon, such as amyloid or tau tracers for assessment of Alzheimer's disease. Many new tracers are under development and the range of research applications continues to expand, which places increased demand on the performance of the instrumentation and the accuracy of the data quantitation. This article reviews the basic principles of PET and the capabilities of current instrumentation, followed by a description of the newest technology and methods of image generation for quantitative imaging. Technologically, the most significant advancements in the last decade include the introduction of TOF PET/CT, which further enhances the capabilities for both clinical and research PET applications, and integrated PET/MR systems, which enable new ways to correlate measures of both anatomic and physiological information.

## Basic principles of TOF PET

In PET the signal is produced by the decay of the unstable particle positronium produced when a positron emitted by an unstable PET nucleus combines with an electron in the surrounding tissue. The positronium decays primarily into two coincident 511 keV photons that are detected in time coincidence by the PET scanner. Measurement of the arrival times of any two photons in the PET scanner allows the determination of a coincident event based on the coincidence timing window ($2\tau$). The coincidence timing window is set to cover the full imaging field-of-view that is typically in the range of 60 cm (±2.00 ns) in order to collect all annihilation events from a whole-body (WB) PET system. Detection of a pair of coincident photons in the PET scanner provides an electronic collimation that localizes the emission point to be along the line (line-of-response, or LOR) connecting the two PET detectors. In addition, the location of the emission point on the LOR is approximately determined by the difference in the arrival times ($t_2 - t_1$) of the two photons (Fig. 1A). However, in conventional PET the precision of the measured photon arrival time as defined by the system timing resolution ($\Delta t$) does not provide an accurate localization of the emission point on the LOR, and hence is not used for this purpose during image reconstruction. By assuming a uniform probability for an event location along the length of the LOR lying within the object boundary and collecting data from all LORs in the azimuthal range, it is possible to reconstruct a PET image that represents an estimate of the underlying the radiotracer distribution [1]. The assumption of a uniform probability of event location along a full LOR length leads to noise correlations in overlapping image voxels from multiple LORs (Fig. 1B) and hence impacts the image signal-to-noise ratio (SNR).

In time-of-flight (TOF) PET, the system timing resolution allows a more precise localization of the event along the LOR (Fig. 1C). Ideally, if system timing resolution provides a spatial uncertainty $\Delta x$ ($\Delta x = c \bullet \Delta t/2$, where c is the speed of light in vacuum) along the LOR that is comparable or better than the detector spatial resolution, then image reconstruction can essentially be described as placing events directly in the most likely image voxels. For an average detector spatial resolution of 4.5 mm, this translates into a system timing resolution of 30 ps, which is at least an order of magnitude better than that currently achieved in commercial PET. However, even with system timing resolution in the range of 400–500 ps ($\Delta x$ = 6.0–7.5 cm), the noise correlations during image reconstruction are limited to fewer

voxels as defined by the timing resolution (Fig. 1D) and hence can lead to improved image SNR [2–4] as long as the positional uncertainty Δx is smaller than the size of the activity distribution, or simply compared to the chord length (D) through the body. This relationship will be described in more detail in the subsequent section titled “Benefit of TOF PET.”

## Brief history of TOF PET

The first generation of TOF PET scanners was developed in the early 1980s at several research institutions [5–10] with a primary goal of brain and cardiac imaging with compounds tagged to short-lived radio-isotopes, such as $^{15}$O-water, $^{11}$C-acetate, and $^{82}$Rb. In order to collect a sufficient number of events from the decay of these short-lived radio-tracers, higher activity levels are injected in the patients, leading to increased randoms to true coincidence ratio and higher system deadtime. In this scenario the reduced random coincidences (due to the use of a narrow coincidence timing window) and reduced deadtime (due to the use of a fast scintillator) were additional incentives for utilizing TOF assisted reconstruction to achieve improved image SNR. The early TOF PET systems used CsF and later $BaF_2$ as the scintillator, and achieved system timing resolution in the range of 450–750 ps. These early systems used 1-1 coupling of the scintillator to a single photomultiplier tube (PMT), and hence the timing resolution was determined primarily by the intrinsic scintillator timing properties and the scintillator size, which was in turn defined by the PMT size. Due to the 1-1 coupling nature of these detectors the system spatial resolution was also determined by the scintillator and PMT size. Attempts were made using light sharing techniques in the detector design [11], but these were limited by the low light output of these scintillators. Hence, these early TOF PET systems suffered from reduced sensitivity and poor spatial resolution of these detectors relative to detectors utilizing BGO, which became the standard crystal used in Non-TOF PET. With the subsequent transition of PET imaging to primarily $^{18}$F-FDG oncology studies, the benefit of TOF PET with these early scintillators could not help overcome the reduced sensitivity and worse spatial resolution. Hence, the 1990s saw PET system design dominated by Non-TOF scanners primarily using BGO crystals with septa for 2D data acquisition [12,13], or alternately using large NaI(Tl) crystals without septa for fully-3D data acquisition [14,15].

## Current state-of-art PET scanners

Lutetium oxy-orthosilicate ($Lu_2SiO_5$(Ce), or LSO(Ce)) was first introduced as a PET scintillator in the early to mid 1990s [16], providing faster decay times and higher light output compared to BGO, which was the primary scintillator being used in commercial PET at that time. LSO was first used in a small animal PET scanner (MicroPET) [17] and subsequently incorporated into a brain scanner [18,19] and finally a whole-body PET scanner (ECAT Accel) [20]. The improved properties of LSO provided higher sensitivity, improved spatial resolution, reduced deadtime and random coincidences, and also helped facilitate the use of fully-3D PET (no septa) as the standard design for modern PET systems [21]. Soon it was also recognized that the very good timing resolution of LSO and another similar scintillator lutetium–yttrium oxy-orthosilicate ($Lu_{1.8}Y_{0.2}SiO_5$(Ce), or LYSO(Ce)) could be utilized in the development of TOF PET systems [22,23] without the limiting design trade-offs present in the first generation TOF PET systems of the 1980s. In 2005,

Siemens presented results from a prototype LSO PET system that achieved a system timing resolution of 1.2 ns using photomultiplier tubes (PMTs) and electronics that were designed for Non-TOF applications [24]. Very soon after this prototype demonstration, the first commercial TOF PET/CT (Philips Gemini TF) system using a lutetium-based scintillator was introduced by Philips that achieved a system timing resolution of 585 ps using LYSO crystals [25]. Currently all three major PET vendors have at least one version of a TOF PET/CT system available, with Siemens using LSO, while Philips and GE use LYSO or another lutetium-based scintillator, respectively. The timing resolution for all of these systems (Philips Ingenuity, Siemens mCT, and GE Discovery 690) is in the range of 500–550 ps using 20–25 mm long crystals [26–28]. In addition to these three major PET vendors, Toshiba has recently introduced the Celesteion PET/CT system, which achieves a system timing resolution of ~400 ps while also using LYSO crystals [29]. A primary reason for the improved timing resolution of this system relative to the PET/CT systems from the other major manufacturers is due to the use of shorter (12 mm long) crystals. In summary, the common theme in all these PET scanners is the use of lutetium-based scintillators, PMTs as the primary photo-sensors, and achievement of system timing resolution in the range of 400–550 ps. While similar timing resolution was achieved in the first generation of TOF PET scanners developed in the 1980s, it is worth repeating that the current generation of TOF PET scanners achieves this performance in addition to a much better combination of spatial resolution and sensitivity. In addition these newer commercial TOF systems have stable calibrations and have demonstrated reliable performance. As we describe later, new hardware developments, especially in the area of photo-sensor technology, are quickly pushing these performance metrics to improved levels and new system designs are being reported with much improved TOF resolution.

## Benefit of TOF PET

In the 1980s significant work was done in estimating the benefits of TOF PET imaging. For a simple, uniform activity distribution it was shown that TOF PET leads to a relative signal-to-noise ratio (SNR) gain of $\sqrt{(\frac{D}{\Delta x})}$, where D is the size of the object being imaged [2,3]. Due to the Poison nature of PET data, this translates into a sensitivity gain of D/Δx. This derivation of sensitivity gain is valid for an analytic image reconstruction algorithm and is not directly applicable to iterative reconstruction methods such as the maximum-likelihood expectation-maximization (MLEM) [30] or ordered-subsets expectation–maximization (OSEM) [31] algorithms. Further, this derivation assumes a system timing response that is rectangular in shape with a width of Δt. A refined estimate of the gain in relative sensitivity from TOF PET was first derived by Tomitani [4] (and subsequently verified by others [32,33]) where he showed that this gain is given by D/(1.6* Δx) under the condition that Δx is greater than or equal to twice the detector spatial resolution. Further work in the 1980s also showed that the sensitivity gain due to TOF as defined by the above formula increases as a function of activity level due to the reduced impact of random coincidences in TOF images [34,35]. In recent years, Conti [36] has further expanded these ideas to consider the gain in Noise Equivalent Count (NEC) coincidences [37] for fully-3D PET, and hence the gain in effective sensitivity due to TOF PET.

While metrics such as relative gain in sensitivity or NEC provide a good starting point for understanding the potential benefits of TOF, these metrics provide only a global measure of improvements in image quality and, more importantly, are more relevant to images reconstructed with analytical reconstruction algorithms such as filtered backprojection (FBP). All modern PET scanners, including the TOF system, use iterative reconstruction algorithms with system modeling of physical effects. Consequently, the choice of number of iterations used for reconstructing the image, and also the effect of different data correction schemes, is not fully represented by metrics such as the NEC. Consequently, significant work has been done in recent years with task-dependent metrics to better understand the impact of TOF PET on clinical images and its effect on clinical imaging protocols, and a detailed description has recently been provided [38]. Briefly, with TOF information the contrast measurement for lesions has been demonstrated to converge faster (requires fewer iterations of the reconstruction algorithm to achieve maximal contrast) both in phantom studies and patient evaluations [24,39–45]. Since fewer iterations of the reconstruction algorithm is also correlated with lower image noise, faster contrast convergence leads to advantageous trade-offs between lesion contrast, image noise, and scan time that affects the quality and quantitative accuracy of the reconstructed images. As an example, in Fig. 2 we show reconstructed transverse slices from a clinical $^{18}$F-FDG patient study. The same data set is reconstructed with TOF and Non-TOF algorithms. After 3 iterations, the TOF reconstruction algorithm converges to a more accurate standardized uptake value (SUV) that changes very little after 10 iterations. The Non-TOF algorithm requires 10 iterations to provide an accurate SUV. However, both TOF and Non-TOF images also show increased noise in the images for 10 iterations, indicating the improved noise and SUV convergence trade-off in TOF images. In summary, the TOF image can achieve lower noise with high lesion contrast, compared to Non-TOF; this can be interpreted as an effective gain in SNR.

Studies have shown that TOF PET leads to: (i) improved lesion detectability [39,42,46–49] while keeping the scan time constant, (ii) reduced scan times [48,49] for the same lesion detectability, (iii) larger gains in lesion detectability for bigger objects [39,42,48,49], (iv) more uniform lesion detectability performance over all patient sizes [49], and (v) reduced variability of lesion uptake measurement over different replicates, different organs, and different patients [50]. All of these studies used metrics that are relevant to oncologic PET imaging. However, the non-linear characteristics of these task-dependent metrics also make it challenging to assign a single gain factor in the resultant images due to TOF information as done in the past and commonly done even today. In Fig. 3 we show qualitatively the benefit of TOF PET in clinical $^{18}$F-FDG imaging. Fig. 3A shows an average size patient (83 kg) study reconstructed (left to right) without TOF information using all counts, with TOF information using all counts, and with TOF information using 1/3 the collected counts. While TOF imaging does not improve the quality of the PET image, the image on the right shows that with TOF information the number of counts (and hence, the scan time) could be reduced without degrading the imaging performance. In Fig. 3B we show an image of a heavy patient (140 kg) without and with TOF information. As indicated by the arrows, the lesion in the TOF image has higher uptake and is also easier to detect compared to the Non-TOF image.

## Factors affecting TOF PET performance and technology advancements

The primary factor affecting the TOF imaging performance of a PET scanner is the system coincidence timing resolution that is determined fundamentally by the choice of scintillator, photo-sensor, and the detector design configured to combine the scintillator and photo-sensor into a position-sensitive PET detector. In addition, the ability to extract the best timing performance using custom electronics that are stable and perform well at high count-rates is also necessary in the design of a state-of-art TOF PET scanner for routine use.

### Scintillators for TOF PET

A good comprehensive summary of PET scintillators capable of good timing resolution has been published previously [51,52]. Here we focus on a smaller group of scintillators that have in recent years either demonstrated their high performance for TOF PET or promised similar capability in the near future. Table 1 summarizes the intrinsic performance characteristics of these scintillators, together with $BaF_2$ and CsF that were originally used in the first generation of TOF PET scanners. We do not list timing resolution numbers here primarily because it is difficult to directly compare measurement numbers from different studies due to variations in scintillator size and the type of photo-sensor used for measurement. In general, timing resolution depends on the statistical quality of the signal in the early part of the scintillation process, which improves as the amount of light in the early part of the signal increases. Hence, for a fixed crystal size and photo-sensor, timing resolution is proportional to the ratio of light output to the signal decay time assuming a similar signal rise-time.

As described earlier, the Cerium doped LSO and LYSO scintillators represent scintillators currently being used in most state-of-art commercial whole-body PET scanners. This is due to a combination of high stopping power (increased system sensitivity), high light output (good spatial and energy resolution), and short decay time (low deadtime). All these characteristics make these scintillators a very good choice for use in fully-3D PET scanners [21]. The combination of high light output, short decay time, and fast rise time also leads to very good timing resolution [22,23] and hence the application for TOF PET imaging. In recent years the Cerium doping process in LSO has been optimized and, in particular, a co-doped version of LSO using Calcium has been developed with increased light output and shorter decay time than the LSO(Ce) scintillator [53], leading to further improvements in timing resolution [61]. Similarly, Calcium and Magnesium co-doped versions of LYSO have also been reported to produce higher light output than Cerium doped LYSO [62]. Another alternative lutetium based scintillator is lutetium fine silicate (LFS-3) [55] that has properties similar to LSO and LYSO and indicates good performance for TOF PET. Recently, cerium doped $Lu_{1.9}Gd_{0.1}SiO_5$ (LGSO) crystals have also been reported [56], which provide a good combination of scintillator characteristics for TOF PET. Thus, there is potential for improved lutetium-based scintillators that could be a direct replacement for current commercial use of LSO and LYSO. There are other new scintillators with different properties that also have potential for TOF systems. Lanthanum halide scintillators and in particular lanthanum bromide ($LaBr_3$) have much higher light output and shorter decay time than LSO(Ce) and LYSO(Ce) [63], leading to improvements in timing resolution [64,65]. In

addition, it was demonstrated by Glodo et al. [57] that increasing the Cerium dopant concentration leads to faster rise times (with minimal loss in light output or change in decay time) and improvements in timing resolution [66]. At the limit of increased cerium doping is the development of pure cerium bromide ($CeBr_3$), which has the fastest decay and rise times for this group of crystals [67,68]. A research whole-body PET scanner has been developed using $LaBr_3$ crystals with a demonstrated system coincidence timing resolution of 375 ps [69]. One drawback of $LaBr_3$(Ce) and $CeBr_3$ scintillators compared to the LSO and LYSO is the reduced stopping power of the detector leading to interesting trade-offs in the design of a TOF PET system. The last category of scintillators is also the most recently introduced and promise excellent performance comparable to that of LSO or LYSO. These crystals represent Cerium-doped rare earth garnets: $Gd_3Al_2Ga_3O_{12}$ (GAGG) [59], $Gd_3(Al, Ga)_5O_{12}$ (GGAG) [60], and $(Gd, Lu)_3(Al, Ga)_5O_{12}$ (GLuGAG) [60]. In Table 1 we show properties of these scintillators which have favorable performance for fully-3D TOF PET scanners. The interest in garnet scintillators is because they have a cubic structure allowing the use of ceramic techniques for faster crystal growth at a much lower temperature and the ability to fabricate the scintillator in different shapes and sizes without cutting, thereby potentially leading to cost-effective manufacturing. With the increasing cost of lutetium, development of non-lutetium based garnet scintillators may have a cost advantage in the long term.

## Photo-sensors for TOF PET

The primary photo-sensor currently being used for conversion of the optical photon signal from the scintillator into electrical signals is the photomultiplier tube (PMT). The primary factors affecting the timing performance of a PMT are: (i) the photo-cathode quantum efficiency (QE), which is the efficiency with which incident scintillation photons are detected and converted into photo-electrons; (ii) the PMT rise time, which defines the response time of the PMT to the detection of a scintillation photon; and (iii) the PMT transit time spread (TTS), which is primarily due to variations in the photo-electron path length when travelling from the point of emission on the photocathode to the first dynode. These three parameters are crucial for maintaining the precision of scintillation light emission temporal behavior. High QE leads to good statistical quality of the signal and improved timing resolution. A fast rise time leads to an overall fast signal rise time and again improved timing resolution. Low PMT TTS reduces the spread in photo-electron arrival time at the anode as a function of the incident position of the scintillation photon on the photo-cathode. The Hamamatsu R4998 (QE = 18% for $\lambda$ = 400 nm, rise time = 0.70 ns, TTS = 0.16 ns, diameter = 25 mm) often serves as a reference for excellent timing performance and therefore has been used for baseline timing resolution measurements. While the intrinsic timing performance of this PMT is superb, the R4998 PMT is too expensive to use in commercial PET scanners that require several hundred to a few thousand PMTs. However, in recent years the commercial introduction of TOF PET/CT has motivated the photomultiplier vendors to develop new fast PMTs with performance close to that of the R4998 and in sizes varying from 19 to 50 mm in diameter and costing a few hundred dollars each. Thus, there is a wider choice of PMTs to the PET/CT vendors who typically use 25 mm or 39 mm diameter PMTs in their detector modules, which typically leads to about 400–800 PMTs for a full system. The most recent developments in PMT technology that have led to even better timing performance are the use of new super and ultra bialkali, plano-concave

photo-cathodes with increased QE and improved dynode structure to improve signal rise time and reduce TTS. For comparison, the typical QE at 400 nm wavelength is ~25% for a standard bialkali photo-cathode, increasing to ~33% for a super bialkali and ~40% for an ultra bialkali photo-cathode [70].

In recent years there has been an introduction of a new solid state photo-detector based on photo-diode technology and variously labeled as silicon photomultiplier (SiPM) or Geiger-mode avalanche photo-diode (GAPD) [71–75]. Each SiPM device typically consists of several thousand micro cells of reverse biased photodiodes operating near breakdown voltage on a common substrate. When a scintillation photon reaches the SiPM surface, it initiates Geiger avalanche in several micro-cells and hence an output signal from the device. An integrated quenching mechanism using a resistor in series with each diode helps limit the device current and enables micro cell recovery. Analog SiPMs operate in a manner where each micro-cell is in parallel with the other micro-cells, leading to a current signal (analog signal) that is proportional to the number of micro-cells firing at any given time. The energy of the scintillation of photon is proportional to the number of micro cells that fire, or the equivalent of integrating the analog signal. Digital SiPMs integrate a dedicated a 1-bit ADC for each micro cell on the substrate, which directly converts the micro cell state (fires or does not fire) into a digital signal [76,77]. Additionally, an on-chip counter (for energy) and timer lead to a fully-digital output of the incident photon energy and timing information. SiPMs have reasonably high photon detection efficiency (PDE) which is a function of the device QE and the density of micro cell packing. Due to the nature of signal production from an avalanche process, SiPMs also have an intrinsic fast rise time and high signal to noise ratio, leading to excellent timing performance and, therefore, can be used for TOF PET. The SiPMs do suffer from energy non-linearity arising from signal saturation effects which are a function of the scintillation photon energy, the device PDE, and the number of micro cells present. Individual SiPMs are typically a few millimeters in size, but large arrays can be fabricated to be useful in TOF PET detectors. Compared to PMTs, SiPM operate at low biasing voltage (few tens of volts), are compact, and can operate in a magnetic field, making them useful for use in TOF PET/MR scanners, as well as TOF PET/CT.

## TOF PET detector design and data acquisition electronics

While the choice of scintillator and photo-sensor represents the fundamental limitations on the timing resolution of a PET detector, the choice of the detector configuration that also provides good spatial resolution and sensitivity has a big impact on the system timing resolution. All intrinsic timing performance measurements are performed by directly coupling a small scintillator directly to a photo-sensor. PET detectors typically use long crystals (e.g., 20–25 mm), with a narrow cross-section (e.g., $4 \times 4$ mm$^2$) arranged in rectangular arrays to large PMTs via a light sharing technique such as that utilized in block detectors [12], quadrant sharing block detectors [78], or the pixelated Anger-logic detectors [79]. Long, narrow crystals suffer light loss as well as some dispersion in transit time of scintillation photons as they undergo multiple reflections within the crystal [22]. In addition, the detector timing resolution further suffers [80] due to the light sharing mechanism where narrow crystals (typically, 4–5 mm wide) are decoded with large PMTs, typically 25–39 mm in diameter. Ideally the best timing resolution with individual crystals is achieved by directly

coupling the crystal to a single channel of a photo-sensor (one-to-one coupling). The one-to-one coupling detector design brings us back to the 1980s when best timing resolution was achieved with ~28 mm diameter PMTs coupled to single CsF or $BaF_2$ crystals of similar size [6]. This was the smallest PMT with excellent timing resolution at that time; since the light output of CsF and $BaF_2$ is low it was not possible to achieve good timing and spatial resolution in a detector; thus, the system spatial resolution of the early TOF systems was relatively poor. While single channel PMTs 4–5 mm in diameter are still not available, multi-anode PMTs such as the H8500 (Hamamatsu) provide a small anode size in a multi-anode structure (8 × 8 for the H8500 with each anode being ~6.25 mm wide) and could be used to directly couple and decode small and long crystals to achieve very good timing resolution [81]. A prototype TOF PET system using a high QE version of the H8500 PMT has been recently developed with coincidence timing resolution of 340 ps [82]. A more practical, and cost-effective alternative to achieve excellent timing with 1-to-1 coupling is the SiPM arrays where each SiPM channel is matched to a single crystal to create larger detector arrays. Alternate to the use of long, narrow crystals is the design of monolithic scintillation detectors readout by a multi-anode PMT or a SiPM array to achieve both good spatial resolution and timing resolution [83,84].

Currently, majority of the commercial PET/CT use a light sharing detector with lutetium-based scintillators (such as LSO and LYSO) and large PMTs (≥25 mm in diameter [26–29]. The system coincidence timing resolution varies between 400 and 550 ps, depending primarily on the scintillator thickness. Recently, scanners using some light sharing with SiPM photo-sensors (2-to-1 ratio of scintillators to SiPM channel) and direct 1-1 coupling of scintillators with moderately cooled digital SiPMs have been introduced, leading to <400 ps and >300 ps coincidence timing resolution respectively [85–87]. Bench-top measurements using 20 mm thick, Ca co-doped LSO monolithic scintillators coupled to a digital SiPM array have demonstrated <200 ps coincidence timing resolution [83]. In parallel, 22 mm thick LYSO scintillators, 1-1 coupled to SiPMs have also shown bench-top measurements of <150 ps coincidence timing resolution [88]. These measurements demonstrate the potential for further improvement for eventual translation to full systems.

Data acquisition electronics for TOF PET scanner typically utilize a leading edge (LE) discriminator or a constant fraction discriminator (CFD) to perform timing pickoff followed by digitization using a time-to-digital converter (TDC) [89,90]. While the LE provides very accurate timing measurement (down to the level of single photons) it can be susceptible to signal noise and/or time slewing due to signal amplitude (energy) variations. The effect of time slewing due to signal amplitude variation is reduced by performing time pickoff at a fixed fraction of the signal amplitude as done in a CFD. Implementation of several hundred channels of high bandwidth CFDs using analog (cable) delays is not practically feasible in modern TOF PET scanners. An important development has been an implementation of non-delay line CFDs in dedicated TOF PET application specific integrated circuits (ASICs) [91–93]. These ASICs also include high precision time-to-digital converters (TDCs) that maintain the precise timing information as well as the additional electronics necessary for acquiring data from the PET scanner.

An alternative to these standard analog or ASIC based signal timing methods is to perform fast waveform sampling (WFS) of the PET detector signals at speeds >1 Gsps. This technique has become affordable and practical with the recent introduction of switched-capacitor-array ASICs such as the Domino Ring Sampler (DRS4) [94,95], and TOF PET data acquisition systems using the DRS4 chips are currently under development for use in research systems with several hundred channels [96]. WFS not only provides improved accuracy of timing measurements but also allows performance of individual channel calibrations, performance of pulse pileup correction at high count-rates, and utilization of sophisticated signal processing techniques to obtain maximal information from the signal pulse. While a data acquisition architecture based on similar WFS techniques is feasible both technically and cost-wise, it is not clear if this technology will be implemented commercially in the near future.

## TOF PET image reconstruction

Early TOF image reconstruction methods were analytical algorithms that made use of the TOF information, including the most likely position (MLP) [2] and confidence-weighted (CW) back-projection [2,4,97,98] algorithms. Subsequently, the iterative MLEM algorithm was adapted to include the TOF probability response function with 2D list-mode data, yielding superior image quality [32,99].

While storing data on an event-event basis (list-mode data) is the most natural way to arrange PET coincidences prior to reconstruction, it is computationally challenging to reconstruct. Hence, binning PET data into sinograms has been traditionally utilized prior to reconstruction. The advent of fully-3D PET together with the use of narrow crystals (for higher spatial resolution) significantly increased the number of LORs and, hence, techniques such as Fourier rebinning were developed to reduce the number of sinogram bins and keep the computational burden manageable. Improvements in computer hardware subsequently allowed the use of sinograms in raw crystal space (no rebinning) to be reconstructed in clinically viable times. The advent of modern TOF PET systems adds another (fourth) dimension to the data, and despite the high sensitivity of these scanners the collected fully-3D TOF PET data for typical clinical studies generally leads to sparse sinograms. Hence, at this point list-mode data acquisition and storage prior to reconstruction is often more efficient than binning into fully-3D TOF sinograms because of the large number of measured LORs with respect to the number of detected events. In addition, list-mode data provide the most flexible format for sorting the data into time frames often required for dynamic imaging protocols. In recent years there have been major developments in list-mode reconstruction methods [100–102], including modeling of TOF information and other physical effects in the system model [103–105]. Faster computers and parallelization over multiple CPUs make a practical implementation feasible today as demonstrated by Wang et al. [106]. Recently there has also been a push towards the implementation of list-mode TOF reconstruction on a fast, off-the-shelf graphics processing unit (GPU) [107] where the fast clock rate and high-bandwidth memory access in a massively parallel processing environment is ideally suited for fast TOF PET image reconstruction.

## Utilization of TOF information for further advancements in PET image reconstruction

Just as fully-3D PET (no septa) acquisition was earlier recognized as providing redundant information that helped improve the statistical noise properties of the reconstructed PET image, TOF information with good timing resolution also provides additional information that helps to localize the annihilation point along an LOR and also provides additional consistency requirements in the image reconstruction process. In particular, it has been recognized by several groups [108,109] that TOF PET images are more robust and less sensitive to errors in data correction techniques (such as normalization, scatter and attenuation correction). These benefits of TOF information are now being utilized in applications such as attenuation correction especially in PET/MR imaging where CT data are not available, improved methods for data calibration, and designing PET systems with a more flexible geometry. Some of these new concepts are described below.

### Simultaneous emission/transmission imaging

A direct benefit of good timing resolution in a TOF scanner is the ability to collect the emission data and transmission data simultaneously. As proposed in Reference 110, a static annular ring of transmission source can be placed within the PET scanner but well beyond the emission imaging field-of-view. During simultaneous emission/transmission imaging, the TOF information allows one to separate events originating within the (emission) FOV from those emitted within the transmission source. The transmission data can then be used to estimate the attenuation correction factors (ACFs) in a manner analogous to the pre-PET/CT days when a rotating $^{68}$Ge source was used to estimate the ACFs [111,112]. The static annular ring of transmission source could in practice also be replaced with a rotating line or several static line sources for transmission imaging.

### Joint emission and attenuation estimation from TOF emission data

Simultaneous attenuation–emission reconstruction approaches have been considered for many years [113], since this avoids the needs for an external transmission (or CT) source altogether. However, for Non-TOF data this type of approach does not provide clinically robust results since the cross-talk between the two reconstructions makes it impossible to uniquely determine both attenuation and emission distributions independently. With the additional information from TOF, simultaneous attenuation–emission reconstruction approaches have been revisited [114]. There are two main approaches that have been proposed for TOF simultaneous reconstruction, maximum-likelihood reconstruction of attenuation and activity (MLAA) and maximum-likelihood attenuation correction factor (MLACF) algorithm, with different performance and implementation tradeoffs. MLAA incorporates joint Maximum-Likelihood estimation of emission and attenuation images, performing alternating emission–attenuation image estimation steps [113,115]. MLACF performs joint estimation of the emission image and attenuation correction factors [116] and is a simple and less computationally complex technique. Although there is a need for a relative scaling of the emission and transmission reconstructions, the cross-talk between them is significantly reduced by incorporating the TOF information into the joint estimation.

A modified algorithm recently proposed uses the background radiation produced by the decay of Lu-176 isotope present in naturally occurring lutetium [117]. The isotope undergoes beta decay to an excited state of Hf-176 followed by a simultaneous cascade of gamma emissions at energies of 307, 202, and 88 keV. As proposed in this work, with appropriate energy and coincidence timing window modifications coincidence TOF data can be acquired for the 307 keV and 202 keV gammas during emission imaging. The reconstructed transmission image is not considered ideal for direct attenuation correction due to low count levels (and contamination from scatter and emission data), but it can potentially be used in a hybrid method to overcome the unknown scaling factor when using the MLACF algorithm.

### Self-calibration of system timing

Maintaining good system timing resolution in a TOF PET scanner requires a careful alignment of the timing signal measured from each event. Factors such as variations in PMT transit times, differences in crystal scintillation behavior, electronic effects such as pulse amplification and signal delay, and variations in the path length of scintillation photons before they reach a PMT photocathode can all lead to a degradation in system timing resolution by adding a bias to the timing signal from each single event. Hence, a timing calibration procedure needs to be routinely performed on TOF PET scanners in order to generate timing offsets on a crystal-by-crystal basis in a PET scanner. This will compensate for timing differences due to the position of the crystal within the detector block, as well as intrinsic differences between crystals. Typically this involves using a singular source (or almost singular such as a point source in a small scatter cylinder) of annihilation events to measure the timing difference for each LOR, where the true value is known. Often an iterative approach is then applied to derive the timing offset for every crystal in the scanner. This technique requires a dedicated calibration source in addition to routine calibration measurements to be performed on the scanner – this can be performed daily before patient studies as part of quality control. Alternatively, as shown recently [118], any data including patient data, can be used with this technique to provide a good estimate of the true TOF difference along a given LOR. Since, some version of timing calibration is always available, the reconstructed patient PET image will be used to refine and to generate a more accurate timing calibration estimate. By using data from multiple patients, timing offsets can be measured and continuously updated with high stability and precision without the need for specialized acquisitions or user intervention.

### Efficiency normalization

Existing normalization correction methods are routinely based on specialized acquisitions of simple phantoms with uniform activity distributions. In order to reduce noise and improve correction uncertainty, labor-intensive high-count acquisitions and accuracy-reducing data smoothing are necessary. Also, even though the data acquisition with phantoms is relatively straightforward, it can be challenging to achieve and maintain image uniformity over time. Based on the observation that TOF reconstruction is less sensitive to errors in efficiency calibration than Non-TOF reconstruction, it has recently been shown that one can determine the detection efficiency correction sinogram on an LOR-by-LOR basis from TOF PET data collected during typical clinical patient scans [119]. In Non-TOF reconstruction, an LOR

with poor detection efficiency cannot be distinguished from low emission activity at locations along the LOR. By utilizing the TOF probability profiles of LORs transverse to a weak LOR, however, TOF reconstruction is capable of detecting and partially compensating for such inconsistencies. Therefore, by forward-projecting a TOF image, a relatively accurate estimate of un-attenuated true event is obtained. Comparison of this sinogram to the measured sinogram can be used to produce an initial estimate of the normalization factors in a manner analogous to the direct inversion techniques. By repeating this procedure iteratively (using the estimated normalization coefficients in the new TOF reconstruction) an accurate measure of the normalization factors can be achieved. Since this technique uses a TOF reconstructed image of any object to obtain the initial estimate, no prior calibration data acquisition is necessary, and clinically one could use the patient data to obtain the normalization sinogram as well as the corrected, reconstructed image.

### Limited angle reconstruction

Another potential benefit of utilizing TOF information PET reconstruction has been explored in the area of limited angle reconstruction where a full PET detector ring may not be available or may be impractical. This application has primarily been evaluated though simulation studies in situations where a partial ring of detectors is used for clinical whole-body PET in order to reduce scanner cost [120], in dedicated breast PET where two PET detectors can be used to image the breast in a flexible geometry [121,122], and finally in proton beam therapy where in-beam PET designs can be used to verify the proton beam range [123,124]. The imaging considerations for both dedicated breast imaging and in-beam proton monitoring influence the design of a split-ring geometry, and limited angular data acquisition. Here we show more generally how TOF information leads to benefits in image reconstruction with incomplete angular sampling. In Fig. 4 we show reconstructed images of a NEMA image quality phantom from data acquired on a clinical whole-body TOF PET/CT scanner, which is composed of 28 flat detector modules in a ring. Data were acquired in list-mode format and reconstructed with all the data (full angular coverage), and also reconstructed with only part of the data, from 20 (~71% angular coverage) and 16 (~57% angular coverage) detector modules. Reconstructed images are shown without and with TOF (575 ps timing resolution) information. As is qualitatively visible, the TOF images for partial singular coverage have reduced artifacts relative to the Non-TOF images, thereby demonstrating the potential to achieve acceptable performance (at least for 70% coverage or greater) in situations where the full angular data may not be available.

## New generation of TOF PET systems

Beyond the PET/CT systems described earlier from the major commercial PET/CT manufacturers, there are other new PET/CT systems coming online from new manufacturers that push the timing resolution to <500 ps, using similar scintillators (LYSO) and conventional photo-sensor technologies (PMT). In addition to Toshiba, two manufacturers based in China have recently reported high performance TOF PET/CT systems. Working in collaboration with University of Texas MD Anderson Cancer Center, Shanghai United Healthcare Co. has reported on its uMI 510 PET/CT system [125]. This system uses 2.54 × 2.54 × 15 $mm^3$ LYSO crystals in a whole-body scanner design with an axial field-of-view

(FOV) of 27.6 cm. The use of very narrow LYSO crystals leads to 2.8 mm reconstructed spatial resolution and 475 ps system coincidence timing resolution. More recently, SinoUnion Healthcare Technologies Co. reported on its PoleStar m660 PET/CT system [126]. This scanner is closer in design specifications to the other commercial PET/CT systems, using $3.63 \times 3.63 \times 20$ $mm^3$ LYSO crystals and having a maximum axial FOV of ~21 cm. The reconstructed spatial resolution of this system is reported to be 3.76 mm and the system coincidence timing resolution is 434 ps.

Beyond PET detector designs using conventional PMTs, the arrival of SiPM has led to a great interest in utilizing these new photo-sensors not only for simultaneous PET/MR systems but also to achieve improved timing resolution in TOF PET scanners. Philips recently introduced the Vereos PET/CT system, which uses digital SiPMs for signal readout from individual LYSO crystals. A combination of shorter crystals (<20 mm), fast timing performance of digital SiPMs, and 1-1 coupling of crystal to a SiPM (no light sharing) leads to a system coincidence timing resolution of ~310 ps [86,87]. In parallel GE developed the SIGNA TOF PET/MR system using a detector ring based on analog SiPMs inserted in the magnet bore, thereby allowing simultaneous PET and MR imaging. With 25 mm thick lutetium-based scintillators, the reported system coincidence timing resolution of this system is 390–400 ps [85]. Hence, while scanners with detectors using conventional PMTs are pushing closer to 400 ps timing resolution, new SiPM technology indicates that system resolution close to 300 ps is achievable with the lutetium based scintillators. As described earlier in the section on TOF PET Detector Design, improvements in both the scintillator performance and the photo-sensor should make it possible to achieve <200 ps TOF in the future.

## Conclusion

Although the principles of time-of-flight imaging have been recognized for several decades, and demonstrated in the early 1980’s with systems developed at academic institutions, it was in the last 10–15 years that the major PET/CT vendors began introducing TOF into their clinical PET/CT systems. An estimated 1/3 of the installed base and the majority of PET/CT instruments being sold today have TOF capability. It is routinely accepted that TOF imaging, together with advanced reconstruction methods, offers significant improvements in the quality of data acquired in PET imaging studies. In particular TOF imaging has led to dramatic improvements in image quality and lesion detectability. TOF has also led to practical benefits, including shorter scans, by taking advantage of the reduction in variance of the reconstructed images. A significant advantage of modern TOF systems is that they incorporate all of the most recent advances in imaging and instrumentation in PET; this includes fully-3D acquisition and image reconstruction from list-mode data, as well as resolution modeling and system modeling to compensate for other physical effects. The practical problems and engineering required for TOF systems were quickly solved so that commercial TOF systems are as reliable and robust as Non-TOF systems, despite the increased complexity. All current commercial TOF PET/CT systems incorporate lutetium-based scintillators, such as LSO and LYSO, and therefore have a combination of inherently high sensitivity and fast timing characteristics, as well as very good spatial and energy resolution required for accurate data quantitation.

The additional information from TOF and improved consistency of TOF reconstruction have been leveraged to improve the data calibrations and accuracy of data correction. TOF also enables both the emission and attenuation to be jointly estimated, which may prove to be a valuable methodology for PET/MR. These hybrid systems currently rely on estimating the attenuation map from the MR images, which is not as accurate as the more direct measurement of the μ-map provided by a CT scanner with PET/CT systems. It is possible to include TOF in a PET/MR system designed for simultaneous imaging, with the PET ring inserted inside the magnet bore, by adapting the PET detector to utilize the new SiPM photo-sensors. These new devices have several advantages; they are compact, have fast timing characteristics, and operate in a magnetic field. Therefore, they can be incorporated into either PET/MR or PET/CT systems, and, in fact, both types of hybrid systems are now commercially available. Since they are compact they can be coupled directly to the scintillation crystal in a 1-to-1 configuration, and thereby achieve excellent timing resolution, along with excellent spatial resolution. In comparison to systems based on conventional photo-multipliers which achieve 400–550 ps, the newer systems based on SiPMs achieve 300–400 ps.

The rapid pace of development of TOF PET/CT systems and integration into the clinic is likely to continue unabated. The benefits of TOF are widely accepted, without any obvious downside. Improvements in performance will continue due to incorporation of new technology, such as SiPM photo-sensors, as well as advances in data correction and image reconstruction algorithms that take advantage of the TOF information. Importantly, the demonstrated value of TOF provides motivation for increased research and development, both in academia and industry, of technology such as new scintillation materials and electronics that promise to advance the performance of TOF PET systems even further.

## Acknowledgments

This work was supported by the National Institutes of Health grant Nos. R01-CA113941 and R01-EB009056.

## References

1. Lewitt RM, Matej S. Overview of methods for image reconstruction from projections in emission computed tomography. Proc IEEE. 2003; 91:1588–611.
2. Snyder DL, Thomas LJ, Terpogossian MM. A mathematical model for positron emission tomography systems having time-of-flight measurements. IEEE Trans Nucl Sci. 1981; 28:3575–83.
3. Budinger TF. Time-of-flight positron emission tomography – status relative to conventional PET. J Nucl Med. 1983; 24:73–6. [PubMed: 6336778]
4. Tomitani T. Image reconstruction and noise evaluation in photon time-of-flight assisted positron emission tomography. IEEE Trans Nucl Sci. 1981; 28:4582–9.
5. Ter-Pogossian MM, Ficke DC, Hood JT Sr, Yamamoto M, Mullani NA. PETT VI: a positron emission tomograph utilizing cesium fluoride scintillation detectors. J Comput Assist Tomogr. 1982; 6:125–33. [PubMed: 6978352]
6. Ter-Pogossian M, Ficke D, Yamamoto M, Hood JT. Super PETT I: a positron emission tomograph utilizing photon time-of-flight information. IEEE Trans Med Imag. 1982; M1-1:179–87.
7. Gariod, R.; Allemand, R.; Cormoreche, E.; Laval, M.; Moszynski, M. Proceedings of IEEE Workshop on Time-of-Flight Emission Tomography. St. Louis (MO): Washington University; 1982. The “LETI” positron tomograph architecture and time-of-flight improvements; p. 25-9.

8. Wong WH, Mullani NA, Philippe EA, Hartz RK, Bristow D, Yerian K, et al. Performance characteristics of the University of Texas TOF PET-I Camera. J Nucl Med. 1984; 25:46–7.
9. Lewellen TK, Bice AN, Harrison RL, Pencke MD, Link JM. Performance measurements of the SP3000/UW time-of-flight positron emission tomograph. IEEE Trans Nucl Sci. 1988; 35:665–9.
10. Mazoyer B, Trebossen R, Schoukroun C, Verrey B, Syrota A, Vacher J, et al. Physical characteristics of TTV03, a new high spatial resolution time-of-tlight positron tomograph. IEEE Trans Nucl Sci. 1990; 37:778–82.
11. Ter-Pogossian MM, Ficke DC, Beecher DE, Hoffmann GR, Bergmann SR. The super PET 3000-E: a PET scanner designed for high count rate cardiac applications. J Comput Assist Tomogr. 1994; 18:661–9. [PubMed: 8040459]
12. Casey ME, Nutt R. A multicrystal two dimensional BGO detector system for positron emission tomography. IEEE Trans Nucl Sci. 1986; 33:460–3.
13. Holte S, Eriksson L, Larsson JE, Ericson T, Stjernberg H, Hansen P, et al. A preliminary evaluation of a positron camera system using weighted decoding of individual crystals. IEEE Trans Nucl Sci. 1988; 35:730–4.
14. Muehllehner G, Karp JS. A positron camera using position-sensitive detectors: PENN-PET. J Nucl Med. 1986; 27:90–8. [PubMed: 3484522]
15. Karp JS, Muehllehner G, Mankoff DA, Ordonez CE, Ollinger JM, Daube-Witherspoon ME, et al. Continuous-slice PENN-PET: a positron tomograph with volume imaging capability. J Nucl Med. 1990; 31:617–27. [PubMed: 2341898]
16. Melcher CL, Schweitzer JS. Cerium-doped lutetium oxyorthosilicate – a fast, efficient new scintillator. IEEE Trans Nucl Sci. 1992; 39:502–5.
17. Cherry SR, Shao Y, Silverman RW, Meadors K, Siegel S, Chatziioannou A, et al. MicroPET: a high resolution PET scanner for imaging small animals. IEEE Trans Nucl Sci. 1997; 44:1161–6.
18. Schmand M, Eriksson L, Casey ME, Andreaco MS, Melcher C, Wienhard K, et al. Performance results of a new DOI detector block for a high resolution PET-LSO research tomograph HRRT. IEEE Trans Nucl Sci. 1998; 45:3000–6.
19. Wienhard K, Schmand M, Casey M, Baker K, Bao J, Eriksson L, et al. The ECAT HRRT: performance and first clinical application of the new high resolution research tomograph. IEEE Trans Nucl Sci. 2002; 49:104–10.
20. Spinks, TJ.; Bloomfield, PM. A comparison of count rate performance for 15-O-water blood flow studies in the CTI HR+ and Accel tomographs in 3D mode. IEEE Nuclear Science Symposium and Medical Imaging Conference; Norfolk (VA). 2002;
21. Muehllehner G, Karp JS, Surti S. Design considerations for PET scanners. Q J Nucl Med. 2002; 46:16–23. [PubMed: 12072842]
22. Moses WW, Derenzo SE. Prospects for time-of-flight PET using LSO scintillator. IEEE Trans Nucl Sci. 1999; 46:474–8.
23. Moses WW. Time of flight in PET revisited. IEEE Trans Nucl Sci. 2003; 50:1325–30.
24. Conti M, Bendriem B, Casey M, Chen M, Kehren F, Michel C, et al. First experimental results of time-of-flight reconstruction on an LSO PET scanner. Phys Med Biol. 2005; 50:4507–26. [PubMed: 16177486]
25. Surti S, Karp J, Werner M, Kolthammer J. Imaging performance of an LYSO-based TOF PET scanner. J Nucl Med. 2006; 47:54P.
26. Jakoby BW, Bercier Y, Conti M, Casey ME, Bendriem B, Townsend DW. Physical and clinical performance of the mCT time-of-flight PET/CT scanner. Phys Med Biol. 2011; 56:2375–89. [PubMed: 21427485]
27. Bettinardi V, Presotto L, Rapisarda E, Picchio M, Gianolli L, Gilardi MC. Physical performance of the new hybrid PET/CT Discovery-690. Med Phys. 2011; 38:5394–411. [PubMed: 21992359]
28. Jeffrey AK, Kuan-Hao S, Anu G, Manoj N, David WJ, Raymond FM. Performance evaluation of the Ingenuity TF PET/CT scanner with a focus on high count-rate conditions. Phys Med Biol. 2014; 59:3843. [PubMed: 24955921]
29. Burr, KC.; Wang, GCJ.; Du, H.; Mann, G.; Balakrishnan, K.; Wang, J., et al. A new modular and scalable detector for a Time-of-Flight PET scanner. IEEE Nuclear Science Symposium and Medical Imaging Conference; Anaheim (CA). 2012;

30. Shepp L, Vardi Y. Maximum likelihood reconstruction for emission tomography. IEEE Trans Med Imag. 1982; 1:113–22.
31. Hudson HM, Larkin RS. Accelerated image reconstruction using ordered subsets of projection data. IEEE Trans Med Imag. 1994; 13:601–9.
32. Snyder DL, Politte DG. Image reconstruction from list-mode data in an emission tomography system having time-of-flight measurements. IEEE Trans Nucl Sci. 1983; 30:1843–9.
33. Wong WH, Mullani NA, Philippe EA, Hartz R, Gould KL. Image improvement and design optimization of the time-of-flight PET. J Nucl Med. 1983; 24:52–60. [PubMed: 6600276]
34. Yamamoto, M.; Hoffman, GR.; Ficke, DC.; Ter-Pogossian, MM. Proceedings of IEEE Workshop on Time-of-Flight Emission Tomography. St. Louis (MO): Washington University; 1982. Imaging algorithm and image quality in time-of-flight assisted positron computed tomography: super PETT I; p. 37-41.
35. Yamamoto M, Ficke DC, Ter-Pogossian MM. Experimental assessment of the gain achieved by the utilization of time-of-flight information in a positron emission tomograph (Super PETT I). IEEE Trans Med Imag. 1982; 1:187–92.
36. Conti M. Effect of randoms on signal-to-noise ratio in TOF PET. IEEE Trans Nucl Sci. 2006; 53:1188–93.
37. Strother SC, Casey ME, Hoffman EJ. Measuring PET scanner sensitivity: relating count rates to image signal-to-noise ratios using noise equivalent counts. IEEE Trans Nucl Sci. 1990; 37:783–8.
38. Surti S. Update on time-of-flight PET imaging. J Nucl Med. 2015; 56:98–105. [PubMed: 25525181]
39. Surti S, Karp JS, Popescu LA, Daube-Witherspoon ME, Werner M. Investigation of time-of-flight benefit for fully 3-D PET. IEEE Trans Med Imag. 2006; 25:529–38.
40. Surti S, Kuhn A, Werner ME, Perkins AE, Kolthammer J, Karp JS. Performance of Philips Gemini TF PET/CT scanner with special consideration for its time-of-flight imaging capabilities. J Nucl Med. 2007; 48:471–80. [PubMed: 17332626]
41. Karp JS, Surti S, Daube-Witherspoon ME, Muehllehner G. Benefit of time-of-flight in PET: experimental and clinical results. J Nucl Med. 2008; 49:462–70. [PubMed: 18287269]
42. Surti S, Karp JS. Experimental evaluation of a simple lesion detection task with time-of-flight PET. Phys Med Biol. 2009; 54:373–84. [PubMed: 19098351]
43. Vandenberghe S, Karp J, Lemahieu I. Influence of TOF resolution on object dependent convergence in iterative listmode MLEM. J Nucl Med. 2006; 47:58P.
44. Lois C, Jakoby BW, Long MJ, Hubner KF, Barker DW, Casey ME, et al. An assessment of the impact of incorporating time-of-flight information into clinical PET/CT imaging. J Nucl Med. 2010; 51:237–45. [PubMed: 20080882]
45. Kolthammer, JA.; Tang, J.; Perkins, AE.; Muzic, RF. Time-of-flight precision and PET image accuracy. IEEE Nuclear Science Symposium Conference record; Knoxville, TN. 2010;
46. Kadrmas DJ, Casey ME, Conti M, Jakoby BW, Lois C, Townsend DW. Impact of time-of-flight on PET tumor detection. J Nucl Med. 2009; 50:1315–23. [PubMed: 19617317]
47. Kadrmas DJ, Oktay MB, Casey ME, Hamill JJ. Effect of scan time on oncologic lesion detection in whole-body PET. IEEE Trans Nucl Sci. 2012; 59:1940–7. [PubMed: 23293380]
48. El Fakhri G, Surti S, Trott CM, Scheuermann J, Karp JS. Improvement in lesion detection with whole-body oncologic TOF-PET. J Nucl Med. 2011; 52:347–53. [PubMed: 21321265]
49. Surti S, Scheuermann J, El Fakhri G, Daube-Witherspoon ME, Lim R, Abi-Hatem N, et al. Impact of TOF PET on whole-body oncologic studies: a human observer detection and localization study. J Nucl Med. 2011; 52:712–19. [PubMed: 21498523]
50. Daube-Witherspoon ME, Surti S, Perkins AE, Karp JS. Determination of accuracy and precision of lesion uptake measurements in human subjects with time-of-flight PET. J Nucl Med. 2014; 55:602–7. [PubMed: 24604909]
51. Lewellen TK. Time-of-flight PET. Semin Nucl Med. 1998; 28:268–75. [PubMed: 9704367]
52. Conti M. State of the art and challenges of time-of-flight PET. Phys Med. 2009; 25:1–11. [PubMed: 19101188]

53. Spurrier MA, Szupryczynski P, Kan Y, Carey AA, Melcher CL. Effects of $Ca^{2+}$ Co-doping on the scintillation properties of LSO:Ce. IEEE Trans Nucl Sci. 2008; 55:1178–82.
54. Pidol L, Kahn-Harari A, Viana B, Virey E, Ferrand B, Dorenbos P, et al. High efficiency of lutetium silicate scintillators, Ce-doped LPS, and LYSO crystals. IEEE Trans Nucl Sci. 2004; 51:1084–7.
55. <http://www.zecotek.com/media/LFS%20White%20Paper.pdf>.
56. Yamamoto S, Okumura S, Kato N, Yeom JY. Timing measurements of lutetium based scintillators combined with silicon photomultipliers for TOF-PET system. J Instrum. 2015; 10:T09002.
57. Glodo J, Moses WW, Higgins WM, van Loef EVD, Wong P, Derenzo SE, et al. Effects of Ce concentration on scintillation properties of $LaBr_3$:Ce. IEEE Trans Nucl Sci. 2005; 52:1805–8.
58. Shah KS, Glodo J, Higgins W, van Loef E, Moses WW, Derenzo SE, et al. CeBr3 scintillators for gamma-ray spectroscopy. IEEE Trans Nucl Sci. 2005; 52:3157–9.
59. Schneider FR, Shimazoe K, Somlai-Schweiger I, Ziegler SI. A PET detector prototype based on digital SiPMs and GAGG scintillators. Phys Med Biol. 2015; 60:1667. [PubMed: 25633017]
60. Wang Y, Baldoni G, Rhodes WH, Brecher C, Shah A, Shirwadkar U, et al. Transparent garnet ceramic scintillators for gamma-ray detection. Hard X-Ray, Gamma-Ray, and Neutron Detector Physics. 2012; XIV:17–18.
61. Szczesniak T, Moszynski M, Syntfeld-Kazuch A, Swiderski L, Koschan MAS, Melcher CL. Timing resolution and decay time of LSO crystals co-doped with calcium. IEEE Trans Nucl Sci. 2010; 57:1329–34.
62. Blahuta S, Bessiere A, Viana B, Dorenbos P, Ouspenski V. Evidence and consequences of Ce in LYSO: Ce, Ca and LYSO: Ce, Mg single crystals for medical imaging applications. IEEE Trans Nucl Sci. 2013; 60:3134–41.
63. van Loef EVD, Dorenbos P, van Eijk CWE, Kramer K, Gudel HU. High-energy-resolution scintillator: $Ce^{3+}$ activated LaBr3. Appl Phys Lett. 2001; 79:1573–5.
64. Surti S, Karp JS, Muehllehner G, Raby PS. Investigation of lanthanum scintillators for 3-D PET. IEEE Trans Nucl Sci. 2003; 50:348–54.
65. Kuhn A, Surti S, Karp JS, Raby PS, Shah KS, Perkins AE, et al. Design of a lanthanum bromide detector for time-of-flight PET. IEEE Trans Nucl Sci. 2004; 51:2550–7.
66. Kyba CCM, Glodo J, van Loef EVD, Karp JS, Shah KS. Energy and timing response of six prototype scintillators for TOF-PET. IEEE Trans Nucl Sci. 2008; 55:1404–8.
67. Shah KS, Glodo J, Higgins W, van Loef EVD, Moses WW, Derenzo SE, et al. $CeBr_3$ scintillators for gamma-ray spectroscopy. IEEE Trans Nucl Sci. 2005; 52:3157–9.
68. Glodo, J.; Kuhn, A.; Higgins, WM.; van Loef, EVD.; Karp, JS.; Moses, WW., et al. $CeBr_3$ for time-of-flight PET. IEEE nuclear science symposium and medical imaging conference; San Diego (CA). 2006;
69. Daube-Witherspoon ME, Surti S, Perkins AE, Kyba CCM, Wiener RI, Karp JS. Imaging performance of a $LaBr_3$-based time-of-flight PET scanner. Phys Med Biol. 2010; 55:45–64. [PubMed: 19949259]
70. <http://www.hamamatsu.com/us/en/technology/innovation/photocathode/index.html>.
71. Buzhan P, Dolgoshein B, Ilyin A, Kantserov V, Kaplin V, Karakash A, et al. An advanced study of silicon photomultiplier. ICFA Instrum Bull. 2001; 23:28.
72. Buzhan P, Dolgoshein B, Filatov L, Ilyin A, Kantzerov V, Kaplin V, et al. Silicon photomultiplier and its possible applications. Nucl Instrum Methods Phys Res A. 2003; 504:48–52.
73. Bisello D, Paccagnella A, Pantano D, Gotra Y, Malakhov N, Jejer V, et al. Metal-resistive layer-silicon (MRS) avalanche detectors with negative feedback. Nucl Instrum Methods Phys Res A. 1995; 360:83–6.
74. Golovin V, Saveliev V. Novel type of avalanche photodetector with Geiger mode operation. Nucl Instrum Methods Phys Res A. 2004; 518:560–4.
75. Renker D. Geiger-mode avalanche photodiodes, history, properties and problems. Nucl Instrum Methods Phys Res A. 2006; 567:48–56.

76. Frach, T.; Prescher, G.; Degenhardt, C.; de Gruyter, R.; Schmitz, A.; Ballizany, R. The digital silicon photomultiplier: principle of operation and intrinsic detector performance. IEEE Nuclear Science Symposium Conference record; Orlando, FL. 2009; p. 1959-65.
77. Degenhardt, C.; Prescher, G.; Frach, T.; Thon, A.; de Gruyter, R.; Schmitz, A., et al. The digital silicon photomultiplier: a novel sensor for the detection of scintillation light. IEEE Nuclear Science Symposium Conference record; Orlando (FL). 2009; p. 2383-6.
78. Wong WH, Uribe J, Hicks K, Zambelli M. A 2-dimensional detector decoding study on BGO arrays with quadrant sharing photomultipliers. IEEE Trans Nucl Sci. 1994; 41:1453–7.
79. Surti S, Karp JS, Freifelder R, Liu F. Optimizing the performance of a PET detector using discrete GSO crystals on a continuous light guide. IEEE Trans Nucl Sci. 2000; 47:1030–6.
80. Moses WW, Ullisch M. Factors influencing timing resolution in a commercial LSO PET camera. IEEE Trans Nucl Sci. 2006; 53:78–85.
81. Krishnamoorthy S, LeGeyt B, Werner ME, Kaul M, Newcomer FM, Karp JS, et al. Design and performance of a high spatial-resolution, time-of-flight PET detector. IEEE Trans Nucl Sci. 2014; 61:1092–8. [PubMed: 25246711]
82. Son J-W, Yoon HS, Won JY, Kim KY, Lee MS, Ko GB, et al. Development and evaluation of a proof-of-concept prototype time-of-flight PET system based on high quantum efficiency multi-anode PMTs. J Nucl Med. 2015; 56:432.
83. van Dam HT, Borghi G, Seifert S, Schaart DR. Sub-200 ps CRT in monolithic scintillator PET detectors using digital SiPM arrays and maximum likelihood interaction time estimation. Phys Med Biol. 2013; 58:3243–58. [PubMed: 23611889]
84. Seifert S, van der Lei G, van Dam HT, Schaart DR. First characterization of a digital SiPM based time-of-flight PET detector with 1 mm spatial resolution. Phys Med Biol. 2013; 58:3061–74. [PubMed: 23587636]
85. Levin, CS.; Glover, G.; Deller, T.; McDaniel, D.; Peterson, W.; Maramraju, SH. Prototype time-of-flight PET ring integrated with a 3T MRI system for simultaneous whole-body PET/MR imaging. Vancouver, Canada. Annual Meeting of the Society of Nuclear Medicine; 2013; p. 148
86. Miller M, Griesmer J, Jordan D, Laurence T, Muzic R, Narayanan M, et al. Initial characterization of a prototype digital photon counting PET system. J Nucl Med. 2014; 55:658.
87. Miller M, Zhang J, Binzel K, Griesmer J, Laurence T, Narayanan M, et al. Characterization of the vereos digital photon counting PET system. J Nucl Med. 2015; 56:434.
88. Ferri, A.; Acerbi, F.; Gola, A.; Paternoster, G.; Zappala, G.; Zorzi, N., et al. 100ps coincidence time resolution with LYSO coupled to NUV-HD SiPMs. San Diego (CA). IEEE Nuclear Science Symposium and Medical Imaging Conference; 2015;
89. Moses WW, Buckley S, Vu C, Peng Q, Pavlov N, Choong WS, et al. OpenPET: a flexible electronics system for radiotracer imaging. IEEE Trans Nucl Sci. 2010; 57:2532–7.
90. Musrock MS, Young JW, Moyers JC, Breeding JE, Casey ME, Rochelle JM, et al. Performance characteristics of a new generation of processing circuits for PET applications. IEEE Trans Nucl Sci. 2003; 50:974–8.
91. Rolo MD, Bugalho R, Gonçalves F, Mazza G, Rivetti A, Silva JC, et al. TOFPET ASIC for PET applications. J Instrum. 2013; 8:C02050.
92. Choong WS, Peng Q, Vu CQ, Turko BT, Moses WW. High-performance electronics for time-of-flight PET systems. J Instrum. 2013; 8:T01006. [PubMed: 24575149]
93. Matsuda H, Kataoka J, Ikeda H, Kato T, Anbe T, Nakamura S, et al. Development of ultra-fast ASIC for future PET scanners using TOF-capable MPPC detectors. Nucl Instrum Methods Phys Res A. 2013; 699:211–15.
94. Ritt, S. Design and performance of the 6 GHz waveform digitizing chip DRS4. IEEE Nuclear Science Symposium and Medical Imaging Conference; Dresden, Germany. 2008;
95. Ronzhin A, Albrow M, Los S, Martens M, Murat P, Ramberg E, et al. A SiPM-based TOF-PET detector with high speed digital DRS4 readout. Nucl Instrum Methods Phys Res A. 2013; 703:109–13.
96. Ashmanskas WJ, LeGeyt BC, Newcomer FM, Panetta JV, Ryan WA, Van Berg R, et al. Waveform-sampling electronics for a whole-body time-of-flight PET scanner. IEEE Trans Nucl Sci. 2014; 61:1174–81. [PubMed: 25484379]

97. Philippe EA, Mullani N, Wong W, Hartz R. Real-time image-reconstruction for time-of-flight positron emission tomography (TOFPET). IEEE Trans Nucl Sci. 1982; 29:524–8.

98. Snyder DL. Some noise comparisons of data collection arrays for emission tomography systems having time-of-flight measurements. IEEE Trans Nucl Sci. 1982; 29:1029–33.

99. Politte DG, Snyder DL. Results of a comparative-study of a reconstruction procedure for producing improved estimates of radioactivity distributions in time-of-flight emission tomography. IEEE Trans Nucl Sci. 1984; 31:614–19.

100. Reader AJ, Erlandsson K, Flower MA, Ott RJ. Fast accurate iterative reconstruction for low-statistics positron volume imaging. Phys Med Biol. 1998; 43:835–46. [PubMed: 9572508]

101. Parra L, Barrett HH. List-mode likelihood: EM algorithm and image quality estimation demonstrated on 2-D PET. IEEE Trans Med Imag. 1998; 17:228–35.

102. Huesman RH, Klein GJ, Moses WW, Qi JY, Reutter BW, Virador PRG. List-mode maximum-likelihood reconstruction applied to positron emission mammography (PEM) with irregular sampling. IEEE Trans Med Imag. 2000; 19:532–7.

103. Kimdon, JA.; Qi, J.; Moses, WW. Effect of random and scatter fractions in variance reduction using time-of-flight information. In: Metzler, SD., editor. IEEE Nuclear Science Symposium and Medical Imaging Conference; Portland (OR). 2003;

104. Popescu, LM. Iterative image reconstruction using geometrically ordered subsets with list-mode data. IEEE Nuclear Science Symposium and Medical Imaging Conference; Rome, Italy. 2004; p. 3536-40.

105. Popescu, LM.; Lewitt, RM. Tracing through a grid of blobs. In: Seibert, JA., editor. IEEE Nuclear Science Symposium and Medical Imaging Conference; Rome, Italy. 2004; p. 3983-6.

106. Wang, W.; Hu, Z.; Gualtieri, EE.; Parma, MJ.; Walsh, ES.; Sebok, D., et al. Systematic and distributed time-of-flight list mode PET reconstruction. IEEE Nuclear Science Symposium and Medical Imaging Conference; San Diego (CA). 2006; p. 1715-22.

107. Pratx G, Surti S, Levin C. Fast list-mode reconstruction for time-of-flight PET using graphics hardware. IEEE Trans Nucl Sci. 2011; 58:105–9.

108. Turkington, TG.; Wilson, JM. Attenuation artifacts and time-of-flight PET. IEEE Nuclear Science Symposium and Medical Imaging Conference; Orlando (FL). 2009;

109. Conti M. Why is TOF PET reconstruction a more robust method in the presence of inconsistent data? Phys Med Biol. 2011; 56:155–68. [PubMed: 21119224]

110. Mollet P, Keereman V, Clementel E, Vandenberghe S. Simultaneous MR-compatible emission and transmission imaging for PET using time-of-flight information. IEEE Trans Med Imag. 2012; 31:1734–42.

111. Daube-Witherspoon M, Carson RE, Green MV. Postinjection transmission attenuation measurements for PET. IEEE Trans Nucl Sci. 1988; 35:757–61.

112. Carson RE, Daube-Witherspoon ME, Jacobs GI, Herscovitch P. Validation of postinjection transmission measurements for PET. J Nucl Med. 1989; 30:825.

113. Panin VY, Aykac M, Casey ME. Simultaneous reconstruction of emission activity and attenuation coefficient distribution from TOF data, acquired with external transmission source. Phys Med Biol. 2013; 58:3649–69. [PubMed: 23648397]

114. Defrise M, Rezaei A, Nuyts J. Time-of-flight PET data determine the attenuation sinogram up to a constant. Phys Med Biol. 2012; 57:885–99. [PubMed: 22290428]

115. Rezaei A, Defrise M, Bal G, Michel C, Conti M, Watson CC, et al. Simultaneous reconstruction of activity and attenuation in time-of-flight PET. IEEE Trans Med Imag. 2012; 31:2224–33.

116. Nuyts, J.; Rezaei, A.; Defrise, M. ML-reconstruction for TOF-PET with simultaneous estimation of the attenuation factors. 2012 IEEE Nuclear Science Symposium and Medical Imaging Conference; Anaheim (CA): IEEE; 2012.

117. Rothfuss H, Panin V, Moor A, Young J, Hong I, Michel C, et al. LSO background radiation as a transmission source using time of flight. Phys Med Biol. 2014; 59:5483–500. [PubMed: 25163423]

118. Werner ME, Karp JS. TOF PET offset calibration from clinical data. Phys Med Biol. 2013; 58:4031–6. [PubMed: 23685837]

119. Werner, ME.; Karp, JS. Detector efficiency calibration from clinical listmode TOF PET data 2014. IEEE Nuclear Science Symposium and Medical Imaging Conference; Seattle (WA). 2014;
120. Vandenberghe S, Lemahieu I. System characteristics of simulated limited angle TOF PET. Nucl Instrum Methods Phys Res A. 2007; 571:480–3.
121. Surti S, Karp JS. Design considerations for a limited angle, dedicated breast, TOF PET scanner. Phys Med Biol. 2008; 53:2911–21. [PubMed: 18460745]
122. Lee E, Werner ME, Karp JS, Surti S. Design optimization of a time-of-flight, breast PET scanner. IEEE Trans Nucl Sci. 2013; 60:1645–52. [PubMed: 24078744]
123. Crespo P, Shakirin G, Fiedler F, Enghardt W, Wagner A. Direct time-of-flight for quantitative, real-time in-beam PET: a concept and feasibility study. Phys Med Biol. 2007; 52:6795–811. [PubMed: 18029976]
124. Surti S, Zou W, Daube-Witherspoon ME, McDonough J, Karp JS. Design study of an in-situ PET scanner for use in proton beam therapy. Phys Med Biol. 2011; 56:2667–85. [PubMed: 21464528]
125. Wong, WH.; Li, H.; Zhang, Y.; Ramirez, RA.; Baghaei, H.; An, S. A high-resolution time-of-flight clinical PET detection system using the PMT-quadrant-sharing technology; St. Louis (MO). Annual Meeting of the Society of Nuclear Medicine; 2014;
126. Huo L, Cui R, Xing H, Li N, Zhu C, Wu H, et al. Performance evaluation of a new high-sensitivity TOF clinical PET/CT system. J Nucl Med. 2015; 56:433.

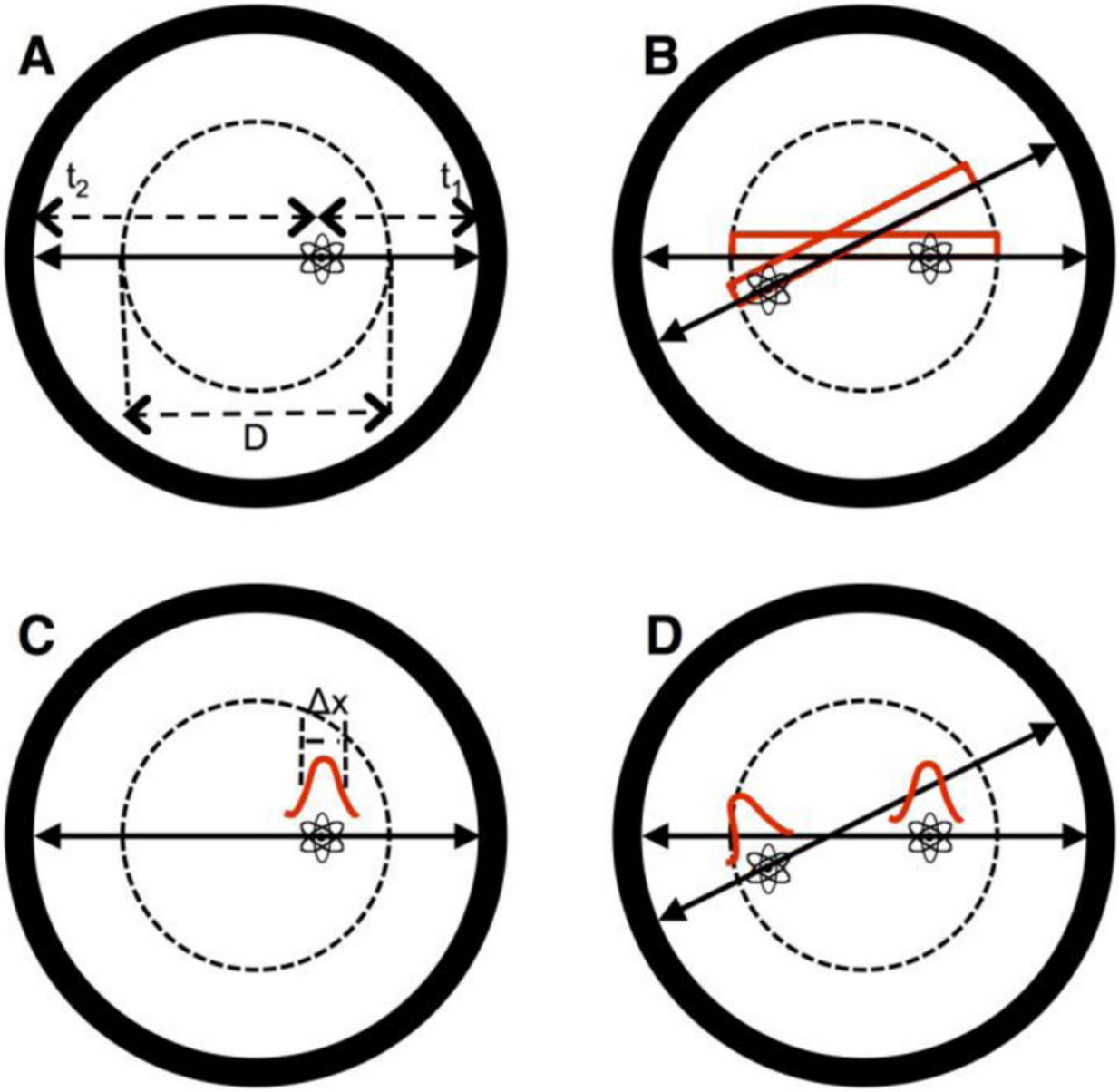


**Figure 1.**

(A) Annihilation point occurring at a distance d from the scanner center within an object of diameter D. The coincident 511 keV photons are detected at times $t_1$ and $t_2$ in the PET scanner. (B) With poor timing resolution in a Non-TOF scanner, a uniform location probability along the LOR within the object is assumed for each annihilation point, leading to noise correlations over a portion of image space following reconstruction. (C) With improved timing resolution in a TOF scanner, the position of the annihilation event is localized along the LOR with a precision that is defined by a Gaussian distribution of width Δx. (D) Improved localization of the two annihilation events along their individual LORs leads to reduced noise correlation (or no noise correlation, as shown here for single LORs) of the events in image space.

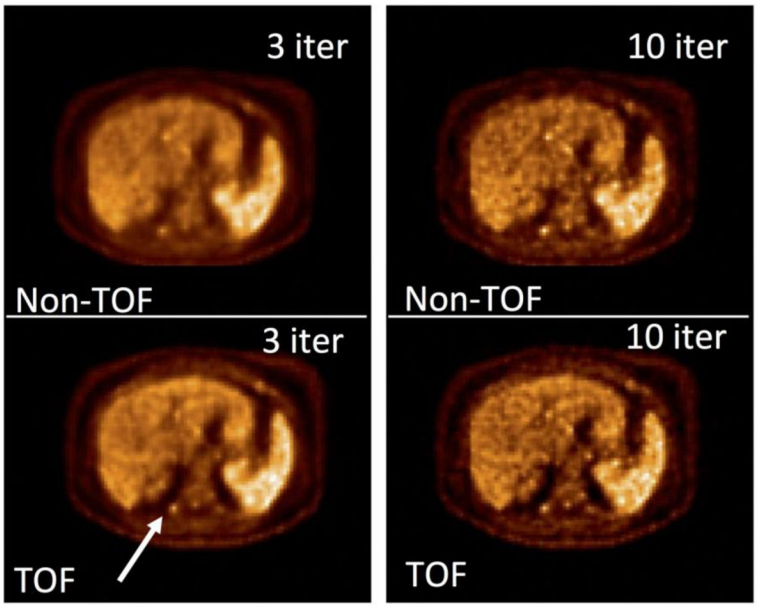


**Figure 2.**

Reconstructed transverse slices of a clinical $^{18}$F-FDG study. As indicated, images are shown for Non-TOF and TOF reconstruction and for iterations 3 and 10 of the reconstruction algorithm. The arrow indicates the lesion for which an accurate SUV is measured after 3 iterations of the TOF reconstruction algorithm.

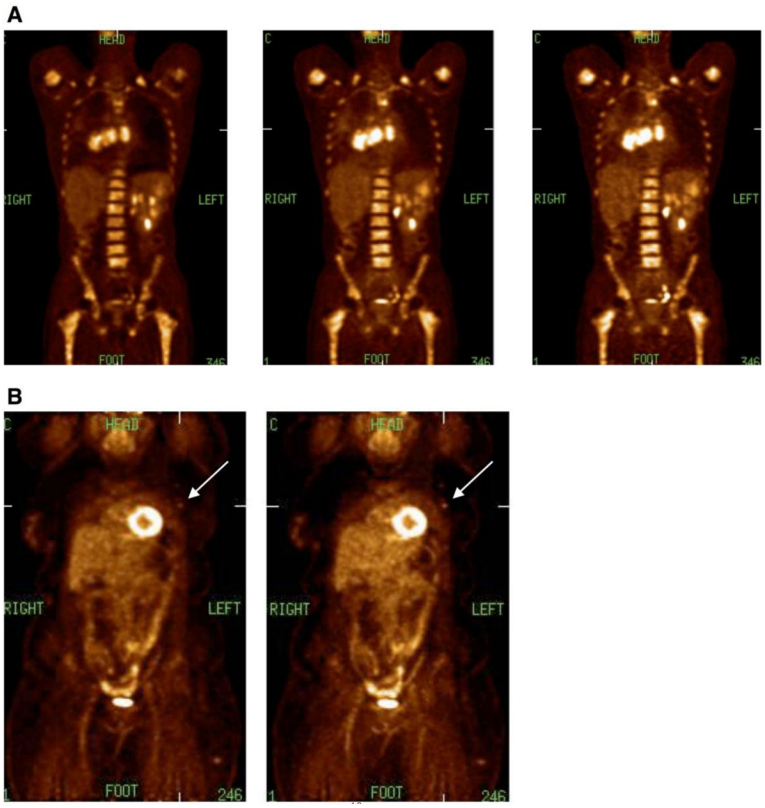


**Figure 3.**

(A) Reconstructed coronal slices of an $^{18}$F-FDG study for an average size (83 kg) patient with a history of metastatic small cell lung cancer. The images shown are (left) Non-TOF reconstruction of all collected counts, (middle) TOF reconstruction of all collected counts, and (right) TOF reconstruction of 1/3 of the collected counts. (B) Reconstructed coronal slices of an $^{18}$F-FDG study for a heavy (140 kg) patient diagnosed with non-Hodgkins lymphoma. The images are (left) Non-TOF reconstruction and (right) TOF reconstruction using all collected counts. Arrows indicate a lesion that has higher uptake and is better discriminated in the TOF image.

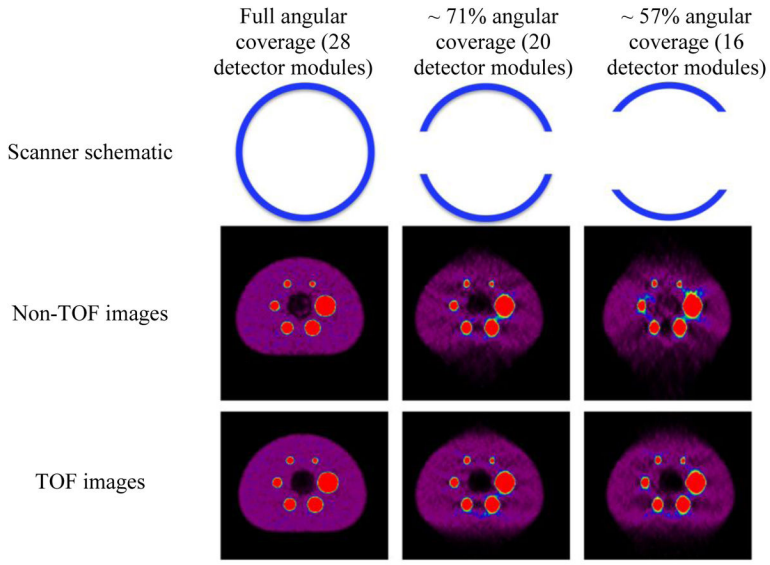


**Figure 4.**

Reconstructed images from a NEMA image quality phantom using full or partial angular data acquired on a clinical TOF PET/CT. The six hot spheres in a ring have diameters of 37, 28, 22, 17, 13, and 10 mm and have an activity uptake of 9.7:1 with respect to background. The central cold region is a lung insert.

**Table 1**

Scintillation properties of selected scintillators appropriate for use in TOF PET. The 511 keV linear attenuation coefficients are shown under the $\mu_{511}$ column. We do not include parameters for Calcium and Magnesium co-doped LYSO since there are not enough consistent data available in peer-reviewed publications yet.

| Scintillator | Density (g/cc) | $\mu_{511}$ ($cm^{-1}$) | Light output (photons/MeV) | Decay time (νσ) |
|---|---|---|---|---|
| LSO [53] | 7.4 | 0.88 | 31,000 | 43 |
| $Lu_{1.8}Y_{0.2}SiO_5$ [54] | 7.1 | 0.78 | 32,000 | 40 |
| LFS-3 [55] | 7.4 | 0.87 | 32,000–34,000 | 36 |
| LSO (Ca co-doped) [53] | 7.4 | 0.88 | 32,000–40,000 | 30–38 |
| LGSO (0.025% Ce) [56] | 7.1 | 0.78 | 28,000 | 33 |
| LGSO (0.1% Ce) [56] | 7.3 | 0.80 | 27,000 | 40 |
| $LaBr_3$ [57] | 5.29 | 0.45 | 61,000 | 15 |
| $CeBr_3$ [58] | 5.2 | 0.39 | 68,000 | 17 |
| GAGG [59] | 6.63 | 0.62 | 46,000 | 88 (92%)<br>230 (8%) |
| GGAG [60] | 6.48 | 0.61 | 65,000 | ~40 |
| GluGAG [60] | 6.80 | 0.64 | 60,000 | ~40 |
| $BaF_2$ [51] | 4.89 | 0.44 | 2,100 (fast)<br>6,700 (slow) | 0.6 (25%)<br>620 (75%) |
| CsF [51] | 4.61 | 0.42 | 2,500 | 2.5 |